Petroleum Science 20 (2023) 3610–3623

Contents lists available at ScienceDirect

Petroleum Science

journal homepage: www.keaipublishing.com/en/journals/petroleum-science

Original Paper

Experimental study on solid particle migration and production behaviors during marine natural gas hydrate dissociation by depressurization

Yan-Long Li [a, b], Fu-Long Ning [b, c], Meng Xu [a, c], Min-Hui Qi [a, b], Jia-Xin Sun [c], Alireza Nouri [e], De-Li Gao [c, d, *], Neng-You Wu [a, b, **]

[a] Key Laboratory of Gas Hydrate, Ministry of Natural Resources, Qingdao Institute of Marine Geology, Qingdao, 266237, Shandong, China
[b] Laboratory for Marine Mineral Resources, Laoshan Laboratory, Qingdao, 266237, Shandong, China
[c] Faculty of Engineering, China University of Geosciences-Wuhan, Wuhan, 430074, Hubei, China
[d] MOE Key Laboratory of Petroleum Engineering, China University of Petroleum, Beijing, 102249, China
[e] School of Mining and Petroleum Engineering, University of Alberta, Edmonton, AB, Canada

ARTICLE INFO

Article history:
Received 31 May 2022
Received in revised form
23 March 2023
Accepted 24 May 2023
Available online 1 June 2023

Edited by Jia-Jia Fei

Keywords:
Natural gas hydrate
Solid particle migration
Sand production
Sand control
Sanding
Hydrate exploitation

ABSTRACT

Sand production is one of the main obstacles restricting gas extraction efficiency and safety from marine natural gas hydrate (NGH) reservoirs. Particle migration within the NGH reservoir dominates sand production behaviors, while their relationships were rarely reported, severely constrains quantitative evaluation of sand production risks. This paper reports the optical observations of solid particle migration and production from micrometer to mesoscopic scales conditioned to gravel packing during depressurization-induced NGH dissociation for the first time. Theoretical evolutionary modes of sand migration are established based on experimental observations, and its implications on field NGH are comprehensively discussed. Five particle migration regimes of local borehole failure, continuous collapse, wormhole expansion, extensive slow deformation, and pore-wall fluidization are proved to occur during depressurization. The types of particle migration regimes and their transmission modes during depressurization are predominantly determined by initial hydrate saturation. In contrast, the depressurization mainly dominates the transmission rate of the particle migration regimes. Furthermore, both the cumulative mass and the medium grain size of the produced sand decrease linearly with increasing initial methane hydrate (MH) saturation. Discontinuous gas bubble emission, expansion, and explosion during MH dissociation delay sand migration into the wellbore. At the same time, continuous water flow is a requirement for sand production during hydrate dissociation by depressurization. The experiments enlighten us that a constitutive model that can illustrate visible particle migration regimes and their transmission modes is urgently needed to bridge numerical simulation and field applications. Optimizing wellbore layout positions or special reservoir treatment shall be important for mitigating sand production tendency during NGH exploitation.

1. Introduction

Natural gas hydrate (NGH) has attracted world attentions as a promising alternative energy since the 1960s (Boswell and Collett, 2011; Liu et al., 2022; Makogon, 2010). Hydrate communities made numerous efforts to evaluate the amount of natural gas stored in NGH, to enhance the NGH reservoir characterization accuracy (Merey, 2019; Riley et al., 2019), and to extract natural gas efficiently (Li et al., 2021a; Lu et al., 2019b; Shen et al., 2021). Potential geomechanical issues during NGH development have proven to be the main obstacles that affect gas production efficiency and safety (Li et al., 2022b; Murphy et al., 2020; Wang et al., 2020; Wu et al., 2022).

* Corresponding author. Faculty of Engineering, China University of Geosciences-Wuhan, Wuhan, 430074, Hubei, China.
** Corresponding author. Key Laboratory of Gas Hydrate, Ministry of Natural Resources, Qingdao Institute of Marine Geology, Qingdao, 266237, Shandong, China.
E-mail addresses: gaodeli@cup.edu.cn (D.-L. Gao), wuny@ms.giec.ac.cn (N.-Y. Wu).

https://doi.org/10.1016/j.petsci.2023.05.018

Sand production, which refers to solid particle migration and discharge into the production well, has been proven to be the most challenging geomechanical response restricting marine NGH development (Hancock et al., 2019; Li et al., 2016, 2019). For example, the NGH production trial conducted in the Nankai Trough of Japan in 2013 was permanently terminated due to severe sand production (Yamamoto et al., 2014; Yoshihiro et al., 2014). The subsequent production trials conducted both in the Nankai Trough (Yamamoto et al., 2019) and the Shenhu area (Li et al., 2017, 2018a; Ye et al., 2020) proved to be affected by sand production. However, they both declared successes in the gas production. Understanding particle migration and production into the wellbore are key to optimizing field operation schedules (Cui et al., 2018; Jin et al., 2022; Li et al., 2020, 2021b).

One of the main challenges in tackling sand production issues is to predict sand production rate quantitatively under different production strategies (Li et al., 2021b; Wu et al., 2021b; Yang et al., 2017). Some simplified numerical simulation approaches were proposed by previous scholars based on some theoretical assumptions (Ning et al., 2020; Wu et al., 2021a). For instance, Uchida et al. (2016) proposed a Thermal-Hydraulic-Mechanical-Chemical (THMC) sand production model under the assumption that the migration of detached solid particles within the porous media is controlled by Darcy's law. The assumption was also applied in the subsequent models proposed by Akaki and Kimoto (2019). Considering possible coupling effects of sand migration and fluid flow during NGH dissociation, some tried to cooperate sand erosion models with the existing NGH production simulators (Liu et al., 2018; Zhu et al., 2020). Another feasible way of simulating sand production behaviors is to integrate commercialized geomechanical simulation codes, either the continuum or discrete element codes, with NGH production simulators (Dou et al., 2020; Li et al., 2018b). However, obtaining a reasonable match between the numerical results and the field data remains a challenge (Dong et al., 2020; Wu et al., 2021b). The reasons include the material characterization challenges and the theoretical assumptions in numerical modeling, which may be inconsistent with real physical processes (Qi et al., 2022).

Laboratory experiments provide insightful evidence to verify the numerical results (Hu et al., 2023; Zhang et al., 2020). Several academic research papers have been published since 2010, after Oyama et al. (2010) pioneered the laboratory experimental test of sand production behaviors during NGH dissociation. A summary of the main features and limitations of experimental testing can be found in our previous publication (Wu et al., 2021a). From the macroscopic and mesoscopic scale, the mass and particle size distribution curves of the sand produced within a certain period were generally used as direct measurements to characterize the behaviors of the sand production during hydrate dissociation (Lu et al., 2019a; Yu et al., 2020). Other monitoring techniques such as acoustic waves (Ding et al., 2019) could be used as supplementary measurements to assess the influences of sand production on the physical properties of hydrate-bearing reservoirs. Various factors such as overlying stress (Fang et al., 2021a; Murphy et al., 2020; Wang et al., 2023), well completion conditions (Fang et al., 2021b; Li et al., 2022a), and fluid flow directions (Dong et al., 2020) were considered in the previous experimental devices.

Han et al. (2018) developed an X-Ray computed tomography imaging-based experimental method from the microscopic scale to obtain particle migration behaviors within the sediment. However, the relationship between particle migration behaviors and sand flow parameters (e.g., mass and size) remains unclear. Optical observation shall provide a bridge between microscopic particle migration and macroscopic sand production to bridge numerical modeling and field applications.

To qualitatively understand the sand production mode during hydrate dissociation, we developed a novel device that can observe particle detachment and migration behaviors from the micrometer to the mesoscopic scales, and test parameters of the produced sand from a macroscopic perspective. Hydrate-bearing samples with different hydrate saturations were prepared and then hydrate was dissociated under depressurization. During this process, sand migration regimes within the sediment were observed using an ultra-deep microscope. The produced sand was collected to measure the masses and particle size distributions. This paper reports these observations and analyzes their implications for marine hydrate exploitation operations.

2. Experiment

2.1. Device and materials

A detailed introduction of the working theories of the experimental device can be found in our previous publications (Jin et al., 2021, 2022). In the previous publication, we discussed sand failure behaviors under low-pressure and ambient-temperature conditions, in which the sediment was free of NGH. The device was updated to satisfy the demand for natural gas hydrate synthesizing and depressurization operation (Chen et al., 2022; Wu et al., 2021a). The schematic diagram of the updated experimental device is shown in Fig. 1. To meet the demand for gas hydrate formation, the vessel is updated into a high-pressure chamber that can withstand an internal pressure of up to 20 MPa. A self-adaptive backpressure module is equipped to meet the demand of depressurization operation. The device also contains a gas-water supply module, a cooling module, a sand collection module, an optical ultra-depth microscope, and a data acquisition and processing module.

The high-pressure chamber comprises a cylindrical vessel body, a top flange, a bottom flange, and a cooling jacket. Six fluid inlets are evenly distributed on the wall of the cylindrical vessel body, and all inlets are located in the middle of the vessel height. A sintered porous ring-shaped plate is equipped inside the vessel. The outer diameter of the ring-shaped plate equals the vessel's inner diameter, and the ring-shaped plate ensures homogenous radial flow into the sediment. A simulated gas production well with a diameter of 1 cm is equipped at the center of the bottom flange. The top flange is equipped with a visible window, allowing direct observation of particle migration within the sediment through the ultra-depth microscope. The outer diameter and height of the simulated hydrate-bearing reservoir are 13 and 2 cm, respectively. The simulated gas production well is packed with gravels to support the wellbore. Two pressure sensors are equipped at the inlet and the outlet of the high-pressure chamber, respectively. A thermometer is inserted into the sediment through a hole equipped in the bottom flange. The distance between the center of the vessel and the thermometer is 4 cm.

Quartz sand with a medium diameter of 49 μm was used in the experiments. Fig. 2 shows the particle size distribution curves of the experimental sediment and typical marine hydrate-bearing reservoir from W18, located in the Shenhu area of the northern South Sea. The average porosity of the sediment is 30%. The uniformity coefficient of the sediment is 3.2, which is within the scope of uniform sand (Li et al., 2017). Methane with a purity of 99.99% and deionized water was used to form methane hydrate (MH). Diameters of the gravels packed inside the simulated wellbore range from 1500 to 1800 μm. It should be noted that the experiments aimed to study particle migration behaviors within the reservoir and its production behaviors without sand control measurement. The gravels packed inside the simulated wellbore were used to support the simulated wellbore solely. The gravel-to-sand

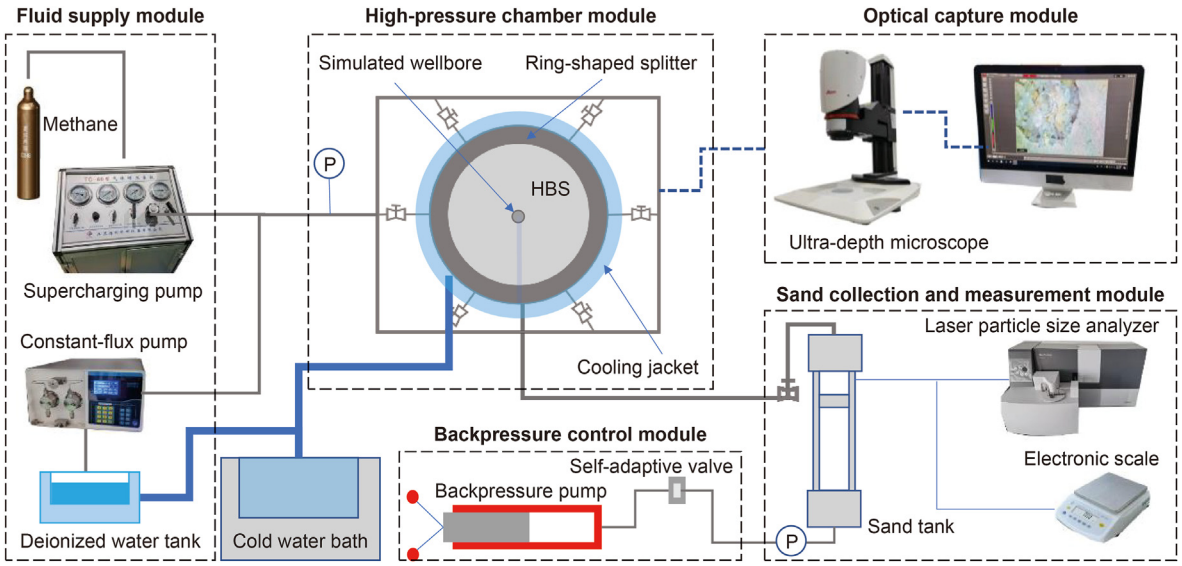

Fig. 1. Schematic diagram of the experimental device.

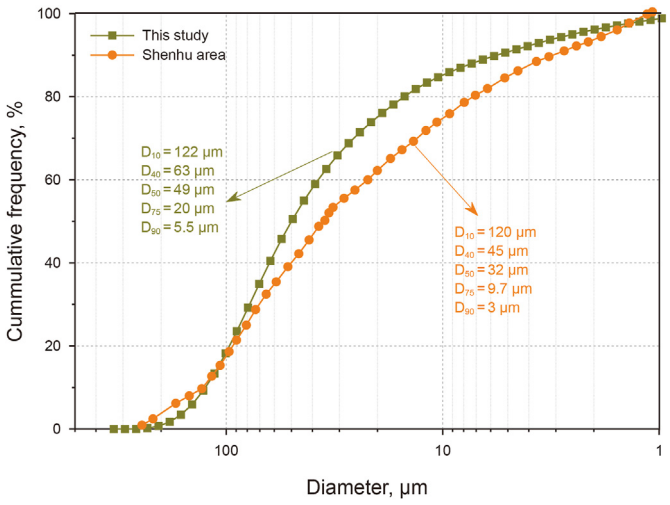

Fig. 2. Comparisons of particle size distributions between this study and typical field cases from the W18 (Li et al., 2020) at the Shenhu area of northern South China Sea.

size ratio is about 30.6–36.7 and such coarse gravels are supposed to be unable to detain fine particles. The sand discharged into the wellbore during depressurization is able to flow out freely and collected for further analyses.

2.2. Experimental procedures

This study considered two variables (i.e., hydrate saturation and depressurization schemes). The experiments were conducted under six representative hydrate saturations of 0%, 7.5%, 15%, 30%, 45%, and 60%, respectively. Five depressurization modes were applied under each hydrate saturation to analyze the relationships between the sand migration regimes and the depressurization rate. As a results, totally 30 experimental scenarios were set in the experiment. At least three repeated experiment were conducted for reliability concerns. Totally 99 experimental rounds were carried out in the paper. A brief description of the experimental procedures are demonstrated below.

First, 200 g of dry sediment were mixed and stirred well with a certain amount of deionized water. All the water molecules added to the sediment were supposed to form hydrates in the experiments. Thus, the amount of required water was calculated by specific volume ratios of methane hydrate and water (i.e., 0.87:1).

Secondly, the mixture was pressed into the chamber and the simulated wellbore was packed with dry gravel. The outer diameter of the wellbore was 1 cm. It should be noted that the mass of gravel packed inside the wellbore was the same for all experiments. The high-pressure chamber was sealed once the sediment and gravel were pressed into a flat. All inlets of fluid remained open during the sediment packing process, whereas the valve downstream of the wellbore remained closed.

The step was followed by pumping methane into the chamber through both the fluid inlets and the simulated wellbore at a relatively low rate. The methane injection process was suspended once the pore pressure reached 6.5 MPa at ambient temperature. This high-pressure ambient temperature state (unable to form MH) was maintained for 2–3 h, and then the cooling module was turned on to cool the chamber to 4 °C.

The MH synthesizing process could be identified by pressure-reduction behaviors during cooling. The MH synthesizing process was supposed to end once the pore pressure remained stable for 8 h at a value higher than hydrate equilibrium pressure. If the pressure approached close to the hydrate equilibrium pressure during cooling, a secondary gas injection circle was conducted to ensure complete water consumption.

After that, another water tank was prepared and the water in the tank was also cooled to 4 °C. The precooled water was injected into the chamber at a very low pump rate of 1 mL/min through the fluid inlets. The backpressure was adjusted and maintained at 5.6–5.8 MPa. Such a water drainage process aimed to displace unhydrated methane, and to assure the sediment was fully saturated with water before depressurization. This ensures a water-saturated HBS environments, which is similar to marine field cases.

The depressurization was implemented by regulating the backpressure module. The depressurization process was suspended when the pressure in the wellbore came to 1.5 MPa. However, the dissociation of MH continued until we could not observe any fluid flow and/or sediment movement from the visual window. The optical microscope was equipped above the visible window on the top flange of the vessel to capture real-time ultra-deep images

during the whole process. The captured images were then used to model sand migration morphological regimes qualitatively.

Finally, the produced sand was collected at the outlet and dried. The mass and particle size distributions of the produced sand were used to characterize the sand production behaviors from a quantitative perspective. Additionally, the PSD characteristics of the remnant sediment in the chamber were also analyzed. The sampling method for the remnant sediment will be discussed in Section 2.3.

2.3. Remnant sediment sampling method

The mass and size of the produced sand were used to characterize the behavior of sand production during development in previous publications (Ding et al., 2019; Dong et al., 2019; Fang et al., 2021a). However, the produced sand could not reflect the particle migration behaviors quantitatively before solid particles were produced into the wellbore. Particle migration within the sediment could cause alterations in local particle sizes. A deep characterization of the remnant sediment might shed light on this problem and benefit numerical modeling.

This study analyzed the particle size distributions of the remnant sediment after depressurization. Samples were collected at different axisymmetric locations adjacent to the well (marked with L1~L3 and R1~R3 in Fig. 3). Three sampling sites were evenly distributed on each side of the well. The sampling process was carried out with a square acrylic sampler, with a length of 1 cm. At least five particle size distribution tests were conducted for each sample.

3. Results and discussions

3.1. Pressure-temperature changes

Examples of the pressure-temperature evolutionary behaviors during sample preparation and MH dissociation are shown in Fig. 4(a) and (b), respectively. The pressure decreases linearly once the cooling process is initiated. The temperature witnesses a sudden rebound, accompanied by a sudden drop in pressure. Both the rebound in temperature and plummet in pressure indicate nucleation and rapid accumulation of MH. MH formation ends when the pressure remains stable for more than 8 h at a value higher than the hydrate equilibrium pressure. The MH saturation in the sample in Fig. 5 is 30%.

During the water inundation process, the pressure in the chamber increases linearly, whereas the temperature remains unchanged (Fig. 4(b)). The water inundation process lasts for 60 min, and it is possible that additional MH would form during the water inundation, causing uncertainties in the experimental results. However, this situation would occur in all experiments and is negligible for lateral comparisons. Typical optical captures before, during, and after water inundation are shown in Fig. 5. It could be seen that the shape of the simulated wellbore remains stable, indicating negligible influences of water inundation on particle migration. Dark-degree changes in the optical captures result from light-reflective capacity differences between water and methane gas.

In Fig. 4(b), we observed a minor difference between the sediment pore pressure and the outlet (i.e., simulated wellbore) pressure once the depressurizing process was initiated. Interestingly, a pore pressure rebound occurs when the outlet pressure comes close to 3.2 MPa, followed by a continuous temperature decrease. The temperature decrease could be viewed as a symbol of rapid MH dissociation. As a result, the pressure rebound is probably caused by the rapid release of methane from MH dissociation, which is unable to dissipate timely. The degree-of-darkness alterations of the optical captures provide evidence for the temporal gas trap in the pores, as shown in Fig. 6. The gap between the sediment pore pressure and the simulated wellbore pressure becomes narrower in the later stage of depressurization. When the pressure in the borehole is reduced from 3.2 to 3.0 MPa, we observe rapid dark-to-light and light-to-dark changes alternately in the optical captures, which is undoubtedly a result of intermittent gas release and expansion. The depressurization is continued until the outlet pressure approaches 1.5 MPa. Optically visible particle migration is observed only when the outlet pressure arrives at 1.6 MPa (marked as the blue line in Fig. 4(b)). Detailed particle migration behaviors will be discussed in Section 3.2.

3.2. Particle migration regimes and their evolutionary modes

3.2.1. Typical particle migration regimes

Particle migration during MH dissociation is a result of sand failure. Visible sand failure was observed only at the late depressurization stage in all experiments. Five sand failure patterns were observed during hydrate dissociation by depressurization, which

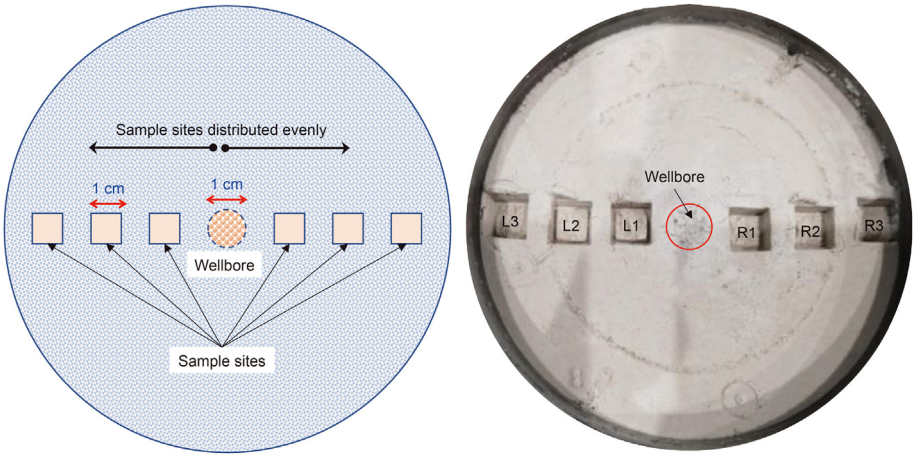

Fig. 3. Schematic diagram (left) and photo (right) of the axisymmetric sampling locations for PSD analyses of the remnant sediment.

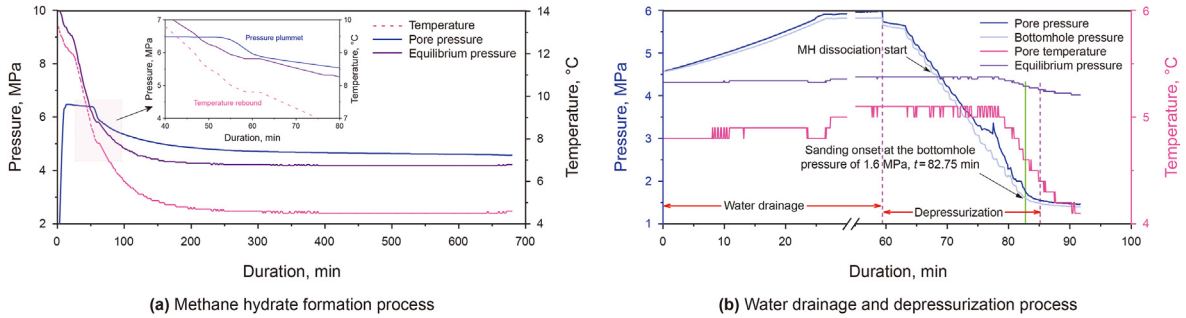

(a) Methane hydrate formation process **(b)** Water drainage and depressurization process

Fig. 4. Typical temperature-pressure changes during hydrate formation, water drainage, and depressurization.

Fig. 5. Optical captures of the simulated wellbore and adjacent HBS before (**a**), during (**b**), and after (**c**) water drainage.

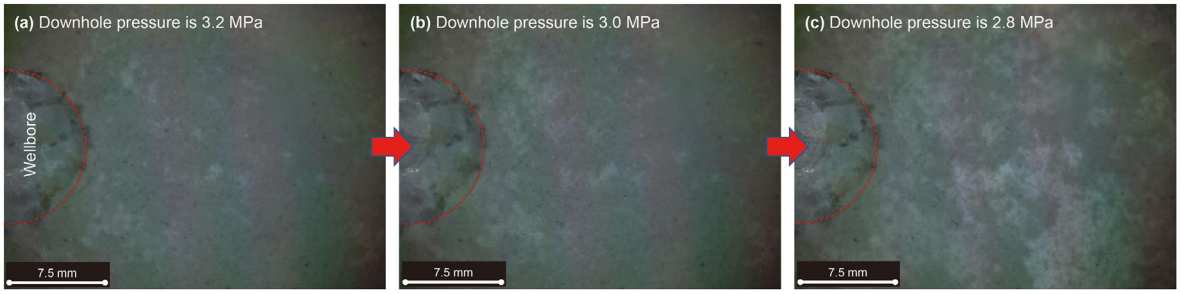

Fig. 6. Typical optical captures when borehole pressure decreases from 3.2 to 2.8 MPa.

are local borehole failure, continuous collapse, wormhole expansion, extensive slow deformation, and pore-wall fluidization.

The optical captures indicated that the sand failure usually initiates around the wellbore in the form of local borehole failures (Fig. 7(a)). When the initial MH saturation is high ($S_h \geq 30\%$), different local borehole collapses tend to aggregate into an overall collapse around the wellbore. Then the margins of the overall collapse gradually expand and extend into the reservoir. The particle migration regime is defined as continuous collapse (Fig. 7(b)).

However, when the initial MH saturation is less than 30%, the tips of local borehole failure would propagate into the reservoir, forming river-like flow channels, which prevent aggregation of local failures. Water and gas mixtures are observed to flow in the flow channels, causing erosion of sand particles at the shoreside of the flow channel. The flow channel is either broadened or deepened due to the detachment and migration of the sand particles. As a result, the structure of the flow channel becomes analogous to that when an earthworm crawls in the soil. Such a sand migration regime is defined as wormhole expansion (Fig. 7(c)).

Extensive slow deformation refers to the phenomenon that the overall sediment in the failure area moves toward the wellbore at a very slow speed. Extensive slow deformation results in some tensile-like fractures that are perpendicular to the direction of fluid flow (Fig. 7(d)). It is observed from the experiments that extensive slow deformation fractures usually occur at the late stage of particle migration. The extensive slow deformation could be evolved from either continuous collapse or secondary wormhole, which will be discussed in Section 3.3.

Pore-wall fluidization refers to the fact that some fine particles migrate within the pore space, while the skeleton of the reservoir remains stable. The pore-wall fluidization cannot be observed via the ultra-deep microscope, but is inferred from analyses of the remnant sediment. In the experiments, we cannot ensure that all sampling sites are located in either the optically visible sand failure areas or the undisturbed areas because the sand failure areas surround the simulated wellbore when the experiments come to an end. Therefore, some of the sampling sites are set in the optically visible sand failure areas, whereas others are not. The location of such mixing sampling sites reflects the overall behavior of particle migration. At the same time, we were unable to distinguish the particle migration of the pore-wall fluidization from those of the optically visible sand failure patterns. The pore-wall fluidization is inferred to occur throughout the depressurization procedures since fluid seepage occurs.

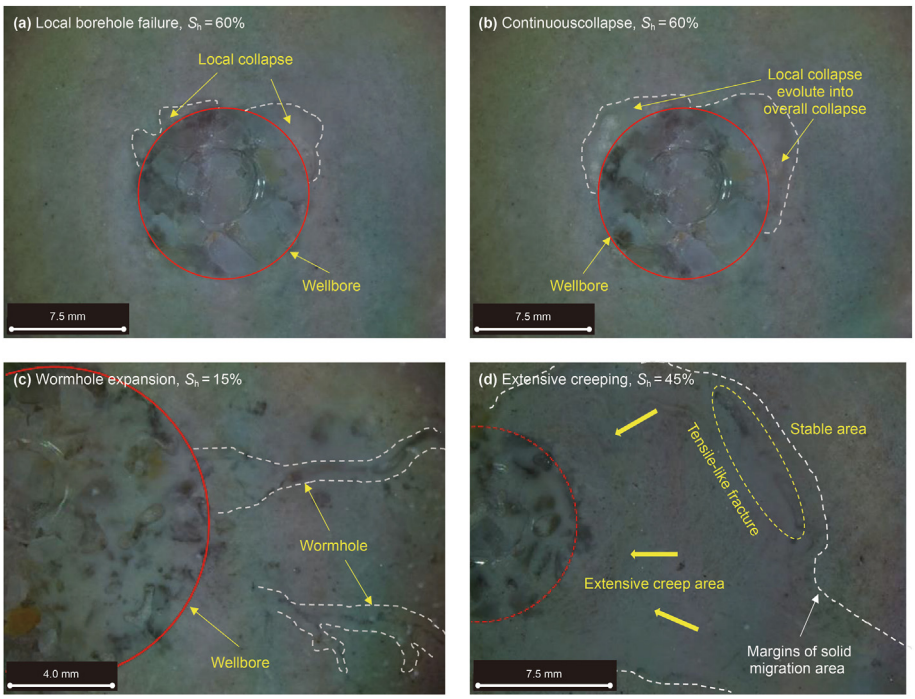

Fig. 7. Typical sand migration regimes during MH dissociation by depressurization.

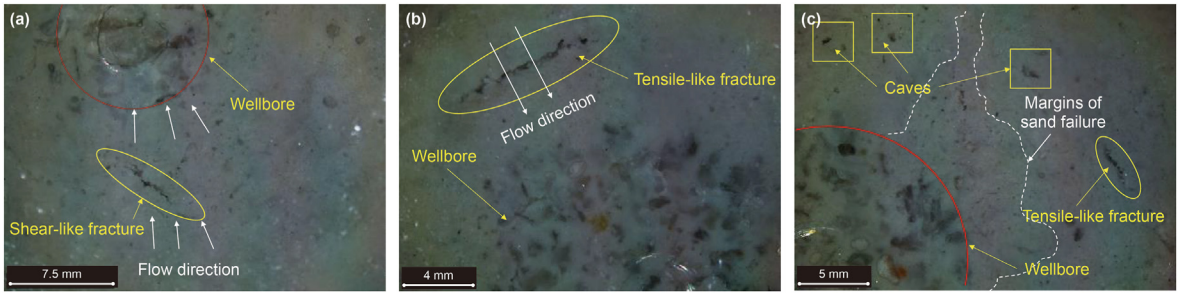

Fig. 8. Fractures and caves occurred outside the margins of sand failure area.

Besides, we also observed pore caves and fractures in the reservoir, as shown in Fig. 8. The propagation directions of the fracture are perpendicular to or inclined to the flow directions, and these fractures are defined as tensile-like fracture and shear-like fracture, respectively. These caves and fractures are not categorized as particle migration regimes, since they usually occur in the stable area (i.e., outside the margins of the visible sand failure area). These reservoir failure morphologies probably result from material depletion. Material depletion during MH production can be induced by both sand outflow and MH dissociation.

3.2.2. Transmission of different particle migration regimes

Once the sand failure occurs, the shape of the sand failure areas grows dynamically with the ongoing MH dissociation. For instance, it is observed that the closure and propagation of the wormhole arise successively during its growth into the formation, namely that the growth of a wormhole is a discontinuous process. This discontinuous process can be attributed to the pressure vibration, which is the result of the combination of discontinuous hydrate dissociation and unsteady two-phase gas-water seepage within the reservoir. Except for the dynamic evolutionary behaviors of the same particle migration regime, we also observed particle migration regime transmissions very interestingly. The transmission modes are mainly dominated by initial MH saturation.

For the cases with relatively high initial MH saturation (S_h = 30%, 45%, 60%, respectively), the local sand failure (Fig. 9(b)) evolves into a continuous collapse (Fig. 9(c)) at the late stage of depressurization. The continuous collapse area extends outward with the ongoing MH dissociation (Fig. 9(d)). The extending process is observed to terminate once the sand failure region exceeds a certain critical value, indicating that continuous collapse would occur only within a limited area adjacent to the wellbore in field cases. A sudden rupture of the sediment is observed at the end of the continuous expansion of the collapse (Fig. 9(e)), resulting in a tensile-like fracture between the continuous collapse area and the surrounding sediment. After that, the sediment within the sand failure area moves toward the wellbore gradually, which is already defined as extensive slow deformation in Section 3.2.1. Extensive slow deformation causes growth of the tensile-like fracture, and sediment outside the sand failure area remains stable. The slow deformation stops when the sand failure area is compacted. However, the subsequent fluid from further MH dissociation still tries to find its way to the wellbore. Therefore, we could observe the occurrence of irregularly shaped wormholes in the sand failure area

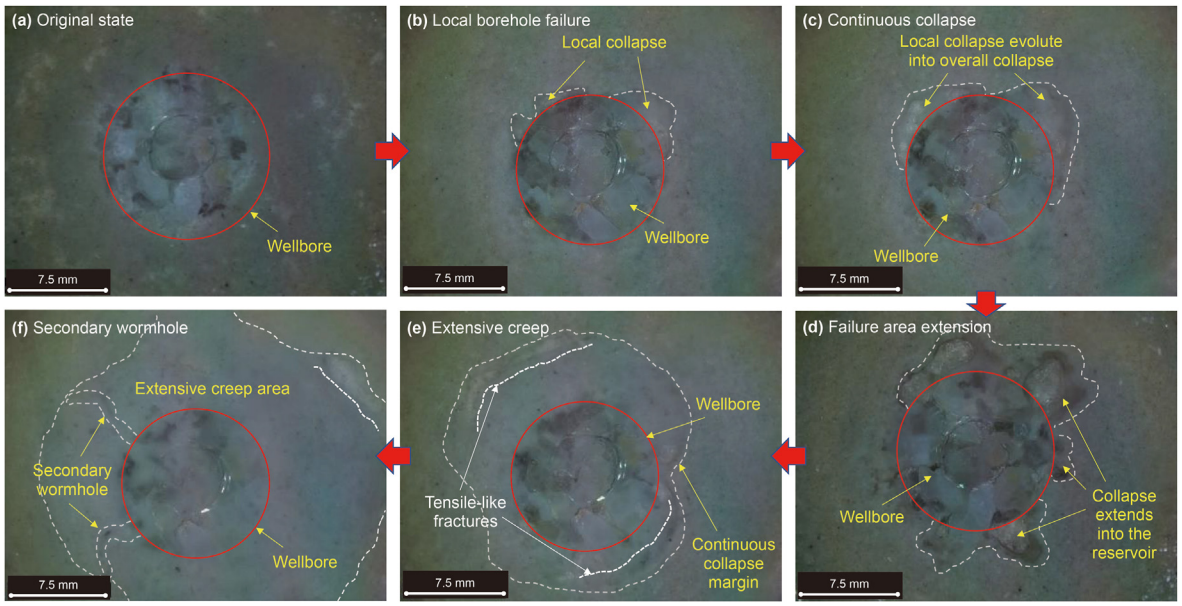

Fig. 9. Particle migration regimes transmission when initial MH saturation is higher than 30%.

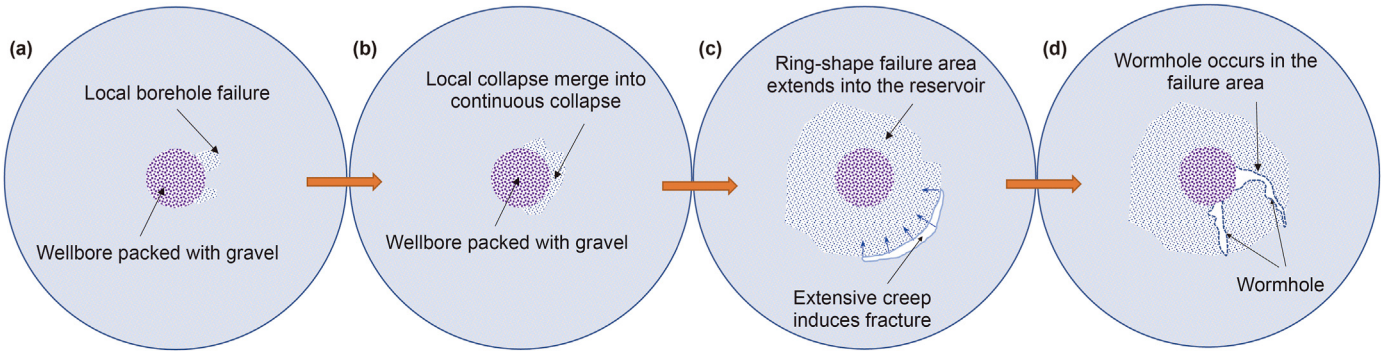

Fig. 10. Idealized particle migration regimes transmission under relatively high initial MH saturation.

(Fig. 9(f)). The shapes of the wormholes change dynamically until the end of fluid flow. The particle migration regimes transmission can be idealized in Fig. 10, where local failure, continuous collapse, extensive slow deformation, and wormholes develop successively during MH dissociation.

When the initial MH saturation is relatively low (S_h = 7.5%, 15%, respectively), the local failure area is smaller than that observed in high-MH saturation cases. Particles at the tips of the local failure area are observed to be detached from the frame during MH dissociation, causing spindle-like extension of the failure area and developing a series of wormholes in the reservoir (Fig. 11(b)). The wormholes extend into the far side of the reservoir, with animated changes in the width, depth, and tortuosity. Interestingly, the tips of the wormholes tend to converge on the far side, and the area trapped by these converged wormholes evolves into an extensive slow deformation (Fig. 11(c)). The previously developed wormholes are buried by deformed sediment. Finally, secondary wormholes develop in the sand failure area and remain open until the end of

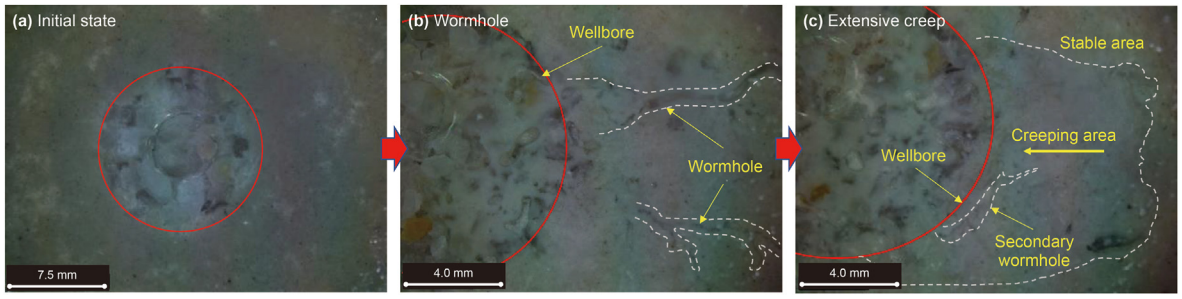

Fig. 11. Particle migration regimes transmission when initial MH saturation is less than 30%.

fluid flow (Fig. 11(c)), in analogy to that observed in the high-MH-saturation cases. It is worth noting that the geometric changes of the secondary wormholes are much slower than those observed in the high-MH-saturation cases. The particle migration regimes transmission can be idealized in Fig. 12, where local failure, wormhole expansion, extensive slow deformation, and secondary wormhole develop successively during MH dissociation.

To sum up, both the continuous collapse and the wormhole expansion originates from local borehole failure. It is observed that the local borehole failure emerges randomly around the wellbore, indicating forces applied to the particles around the wellbore are nonuniformly distributed during hydrate dissociation. The occurrence of the random local failure shall be attributed to both the nonuniform MH dissociation and nonuniform gas-water flow behaviors. On the one hand, MH dissociates nonuniformly in the reservoir, indicating that local strengths of the reservoir also decay nonuniformly, and this, in turn, causes the random distribution of local failure. On the other hand, it was proved by previous scholars that drag forces applied on sand particles by water are higher than that acted by gas by two orders of magnitude (Bedrikovetsky et al., 2012; Qi et al., 2021). Hence, randomly distributed local sand failure enlightens us that the MH dissociated water and gas could barely enter the wellbore in the form of multi-phase flow. Some gas might escape from the water and flows into the wellbore in a separate flow channel.

The differences in the emerging mechanisms of continuous collapse and wormhole expansion could also be attributed to the nonuniform gas-water flow behaviors. The higher the initial MH saturation, the more gas would be released during depressurization. Local failure tends to escalate to continuous failure once the water flow is distributed by excessive gas (i.e., high initial MH saturation). However, the local failure cannot aggregate when MH dissociation released gas cannot fully stir the water flows under relatively low initial MH saturation cases.

It is noteworthy that we also conducted a comparative experiment, in which the sediment was free of MH initially. The depressurization operation is applied under the condition that the sediment is saturated with water and free gas at 5.8 MPa. It is observed that extensive slow deformation occurs once the depressurization is initiated and the sand failure area expands with increasing depressurization amplitude. However, both the continuous collapse and wormhole expansion processes were not observed during the whole depressurization. This phenomenon implies that the existence of MH would inevitably affect particle migration regimes. Only considering the gas-water two-phase flow is insufficient to describe particle migration behaviors in an MH reservoir accurately. A possible inducement of the difference is that the MH dissociation is a process of unsteady gas bubble release. Expansion of the released bubbles causes disturbance of the multiphase flow and induces the occurrence of either continuous collapse or wormhole expansion.

Besides, it is found that the depressurization rate could barely affect the particle migration regimes and their transmission modes under the same initial MH saturation conditions. However, the transmission rate among different particle migration regimes could be prominently accelerated by increasing the depressurization rate. The influences of the depressurization rate on the sand production rate are discussed in the following text.

3.3. Characteristics of produced sand

3.3.1. Influences of hydrate saturation

The cumulative mass and medium grain size of the produced sand during the 60-min depressurization under the same depressurization rate (0.2 MPa/min) are shown in Fig. 13. The following conclusions can be obtained from Fig. 13. First, both the cumulative mass and the medium grain size of the sand produced from the experiments without MH are abnormally higher than those when the sediment contains MH in the initial state. Secondly, the cumulative mass and medium grain size of the produced sand decrease exponentially with the increase in initial MH saturation, except for the cases when the initial MH hydrate is 0%. Most obviously, the medium grain sizes of the produced sand are smaller than those of the original reservoir sediment by an order of magnitude.

The significant influences of initial hydrate saturation on the mass and sizes of the produced sand could be attributed to the gas-water two-phase flow state in the reservoir, which could be confirmed from the optical captures by the visual window. We observed apparent discontinuous gas emission and expansion processes during the MH dissociation. The higher the more likely the initial MH saturation, the water is more likely to be gasified and stirred, and vice versa. Therefore, the two-phase gas-water flow tends to become unsteady slug flow under relatively high MH saturation. In contrast, gas and water are observed to flow in relatively separate flow paths under relatively low MH saturation (Fig. 14). The unsteady slug flow is unfavorable for continuous particle migration, as the gas slug is probably unable to provide enough motivations for particle flow. However, under relatively low initial HM saturations, a steady water flow path enables continuous particle migration throughout the MH dissociation process, which in turn causes an increase in both the cumulative mass and particle size of the produced sand. Namely, steady water flow enhances sand production rate, although the sand failure area in the

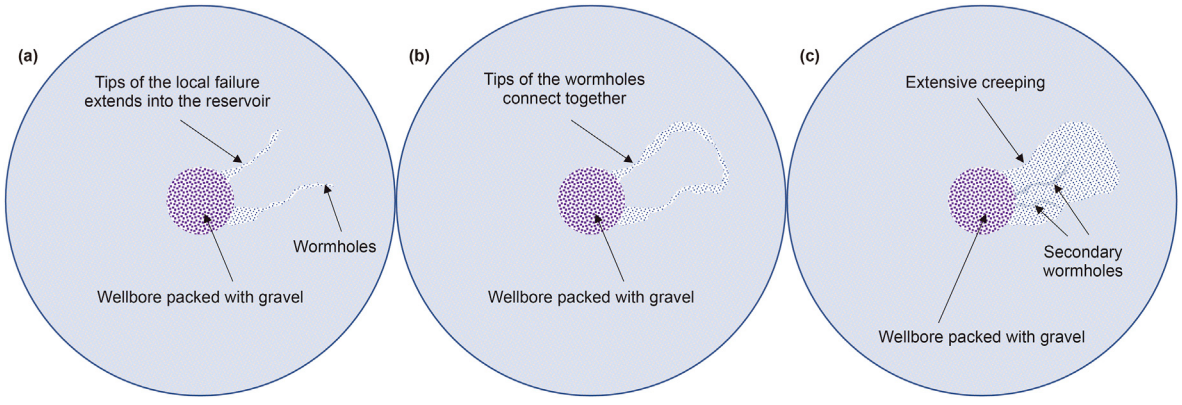

Fig. 12. Idealized particle migration regimes transmission under relatively low initial MH saturation.

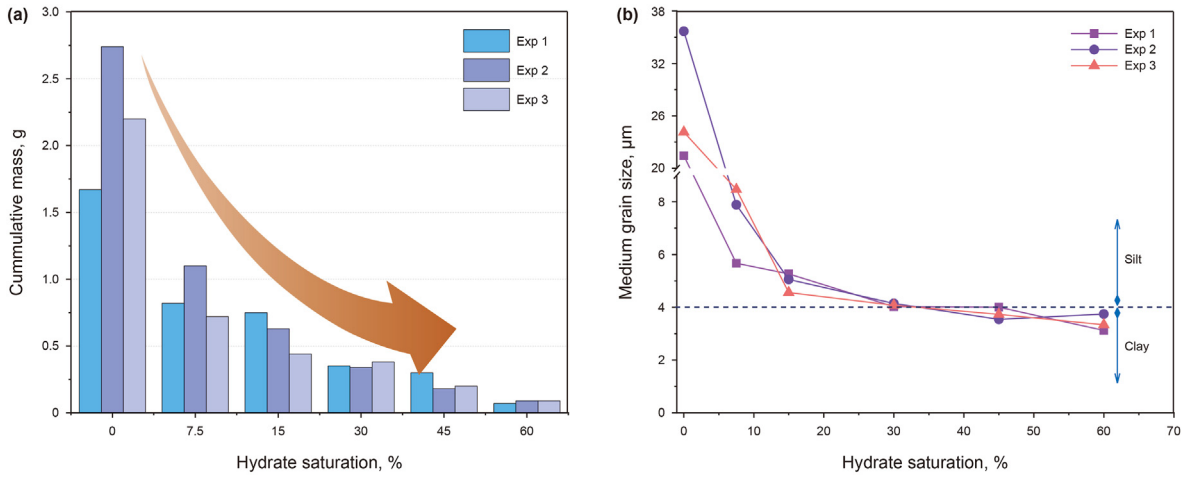

Fig. 13. Changes of cumulative mass (**a**) and medium grain size (**b**) with MH saturation under the depressurization rate of 0.2 MPa/min.

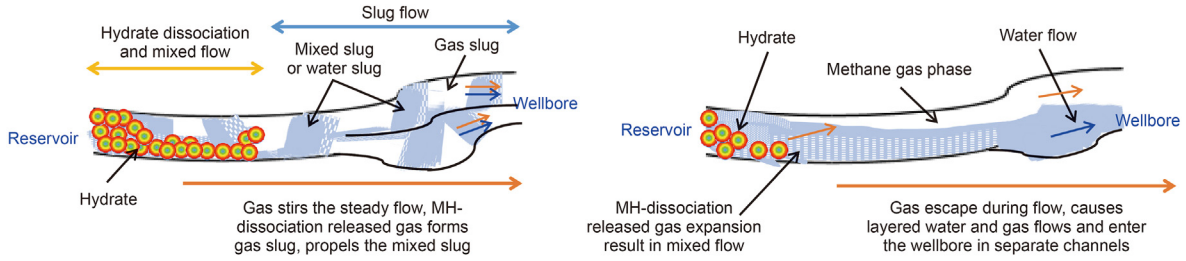

Fig. 14. Possible fluid flow regimes during natural gas hydrate dissociation by depressurization under high hydrate saturation (left) and low hydrate saturation (right) conditions.

formation is relatively smaller under relatively low initial MH saturation conditions.

Fig. 13 also implies that sanding mechanisms for sediment free of hydrate are different from those containing hydrate. This could be attributed to the intermittent expansion and explosion of gas bubbles during MH dissociation (Fig. 15). As stated above, the gas release is discontinuous and the local bubble expansion and explosion shall be unordered and nondirective. As a result, the flow directions of the water and particles are disturbed. The forces applied to the previously flowing particles shall be changed, and thus alters the migration direction. The disturbance in the forces and changes in flow direction shall delay the outflow of solid particles.

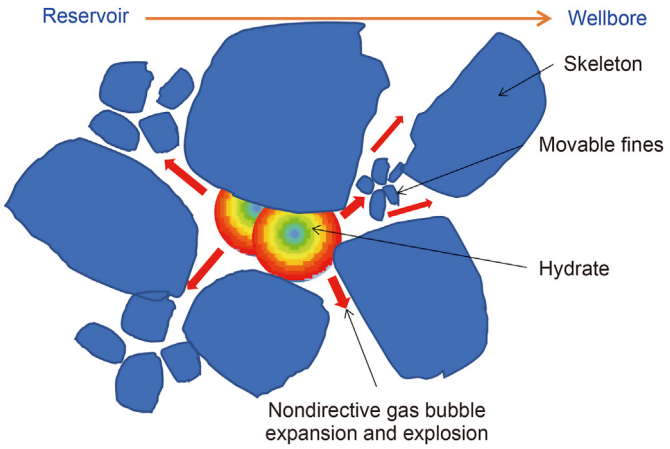

Fig. 15. Unordered and non-directive gas bubble expansion and explosion delays the outflow of solid particles.

In summary, the changing trend of cumulative mass and particle size with MH saturation could be attributed to flow regimes. Continuous water flow is probably the primary inducement of sand production. However, flow regime disturbance induced by bubble emission and explosion would significantly delay sand production. To verify this assumption, we synthesize the MH-bearing sample (S_h = 30%). Depressurization is conducted directly once the MH synthesizing process is completed, without water drainage. Namely that the reservoir is saturated with MH and unhydrated methane. We did not observe any fines produced during depressurization, and the optical captures also did not show the sand failure regimes as mentioned earlier.

3.3.2. *Influences of depressurization rate*

It is found from the optical observation that depressurization rate could barely affect the particle migration regimes, as well as their transmission modes, under the same initial MH saturation conditions. However, the transmission rate of the particle migration regimes could be prominently accelerated by increasing the depressurization rate. A comparison of the cumulative mass and size of the produced sand when initial MH saturation is 30% are shown in Fig. 16. One can observe from the results that the changes in cumulative mass and size of the produced sand are negligible when the depressurization rate increases from 0.2 to 1.0 MPa/min.

The result seems to puzzle us since the previous numerical simulation indicated that an increase in depressurization rate might enhance sand production rate significantly (Uchida et al., 2019; Zhu et al., 2020). The discrepancies between the numerical simulation and the experiments can be ascribed to discontinuous

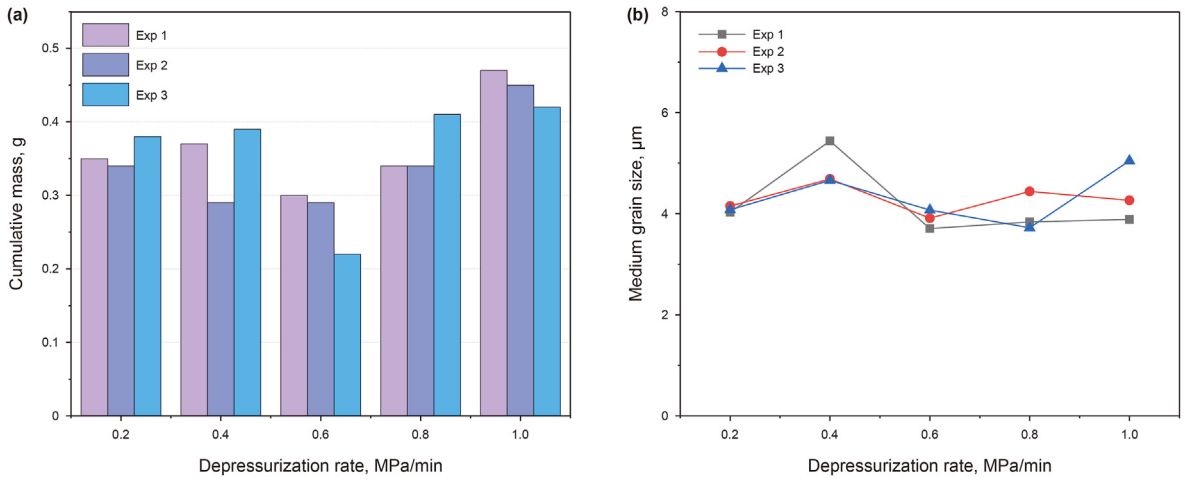

Fig. 16. Cumulative mass and size of the produced sand when initial MH saturation is 30%.

gas bubble emission, expansion, and explosion (Fig. 15).

Another possible inducement of the discrepancies might be hydrate reformation during depressurization. We observed secondary hydrate blocks at the outlet of the wellbore under a depressurization rate of 0.8 (Fig. 17(a)) and1.0 MPa/min (Fig. 17(b)) when the experiments terminated. The secondary hydrate blocks are observed even under a slow depressurization rate (i.e., 0.2 MPa/min) when initial MH saturation is 60% (Fig. 17(c)). This implies that the high initial MH saturation intensifies the occurrence of secondary hydrate blockage, which would undoubtedly hinder the sand production rate.

3.4. Characteristics of remnant sediment

3.4.1. Influences of hydrate saturation

Samples of the remnant sediment after experiments were taken to analyze particle migration behaviors quantitatively, as was stated in Section 2.3. The medium grain size distributions of the remnant sediment under the same depressurization rate of 0.2 MPa/min are shown in Fig. 18. It could be seen that depressurization imposes a sieving effect on the reservoir particles. Hence, the particle sizes of the remnant sediment become higher than that of the original sediment. Under relatively low initial MH saturation (S_h = 0%, 7.5%, and 15%) conditions, the grain size of the remnant sediment increases with the distance to the simulated wellbore. Besides, the difference between the sizes of the original sediment and the remnant sediment is an intensive indicator of particle migration behaviors. Fig. 18 indicates that fines outflow mainly occurs at the near-wellbore area. The sediment at the far side almost keeps station during depressurization when initial MH saturation is low (S_h = 0%, 7.5%, and 15%).

However, the grain size of the remnant sediment decreases with the distance from the sampling locations to the simulated wellbore under relatively high initial MH saturation (S_h = 30%, 45%, 60%, respectively) conditions. It should be strengthened by noting that such a diametrically opposed changing trend never implies that fine migration only occurs at the far-side of the reservoir. It reveals that fine migration occurs in both the near and far side areas during depressurization. However, part of the fines from the far side cannot be produced timely but are detained around the wellbore within the 60-min depressurization.

To sum up, the reservoir component could be redistributed by particle migration during hydrate dissociation. The higher the initial MH saturation is, the larger the fines migration area would be. The particle size distribution modes of the remnant sediment shown in Fig. 17 match the particle migration regimes. Such interesting grain size distribution modes also imply the existence of pore-wall fluidization throughout the experiment, since some of the sampling sites are not located in the optically visible sand failure areas.

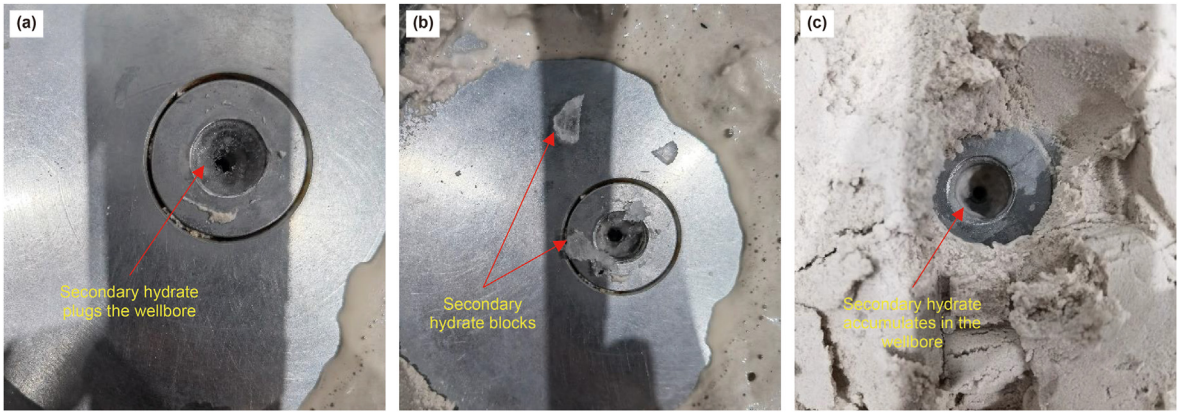

Fig. 17. Hydrate reformation occurs around the wellbore during depressurization.

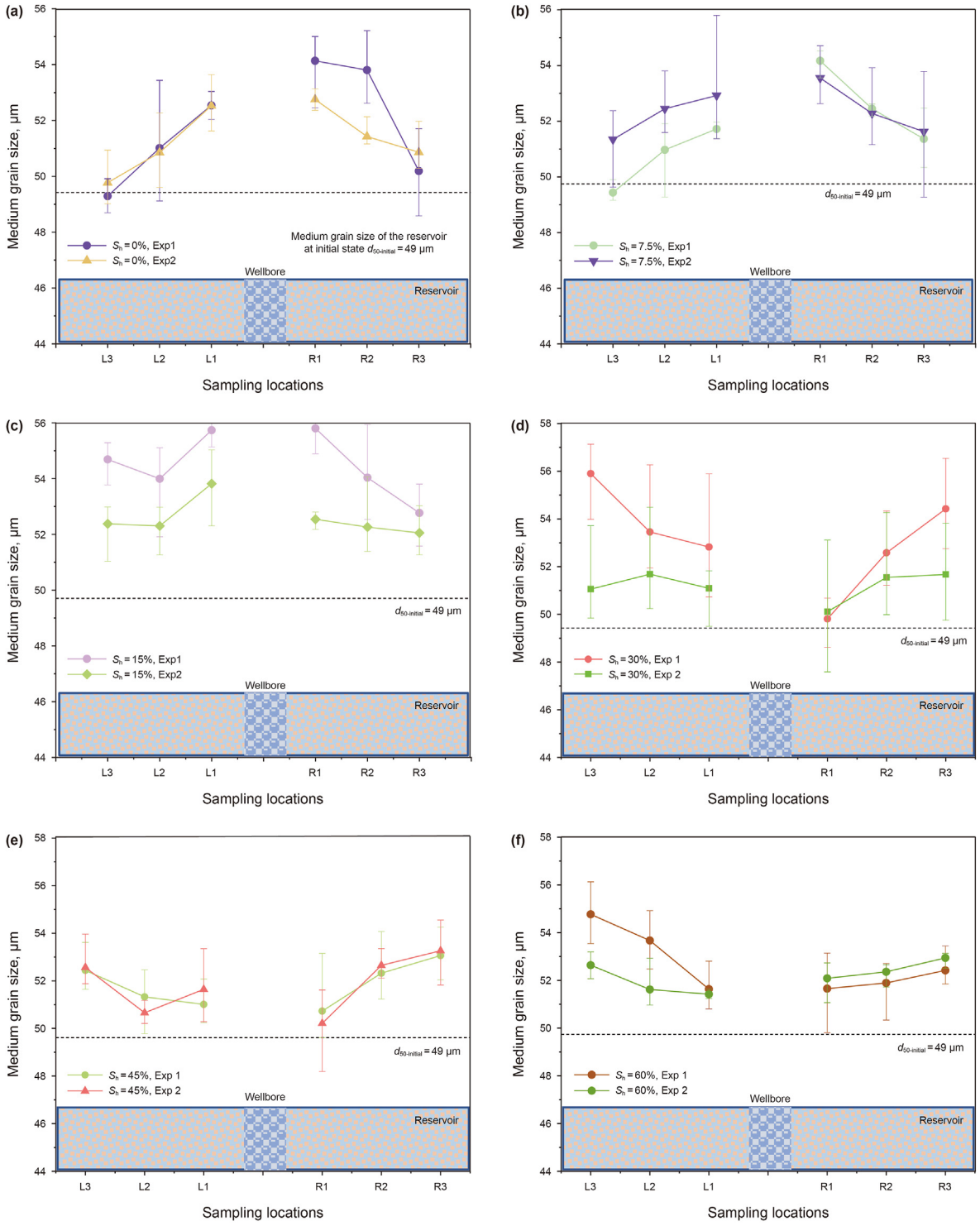

Fig. 18. Particle size distributions of the remnant sediment around the wellbore when the depressurization rate is 0.2 MPa/min.

3.4.2. *Influences of depressurization rate*

The influence of depressurization rate on the remnant particle size distribution can be seen in Fig. 18(d) and 19, when the initial MH saturation is 30%. It could be seen that the grain size of the remnant sediment increases with the distance to the simulated wellbore in all cases. This indicates that the increase in depressurization rate could barely alter the original particle size distribution modes. The occasional alteration of the particle size distribution mode when the depressurization rate is 1.0 MPa/min (see Fig. 19(d)) shall be attributed to hydrate reformation, as was stated previously. The occurrence of secondary hydrate hinders particle migration significantly.

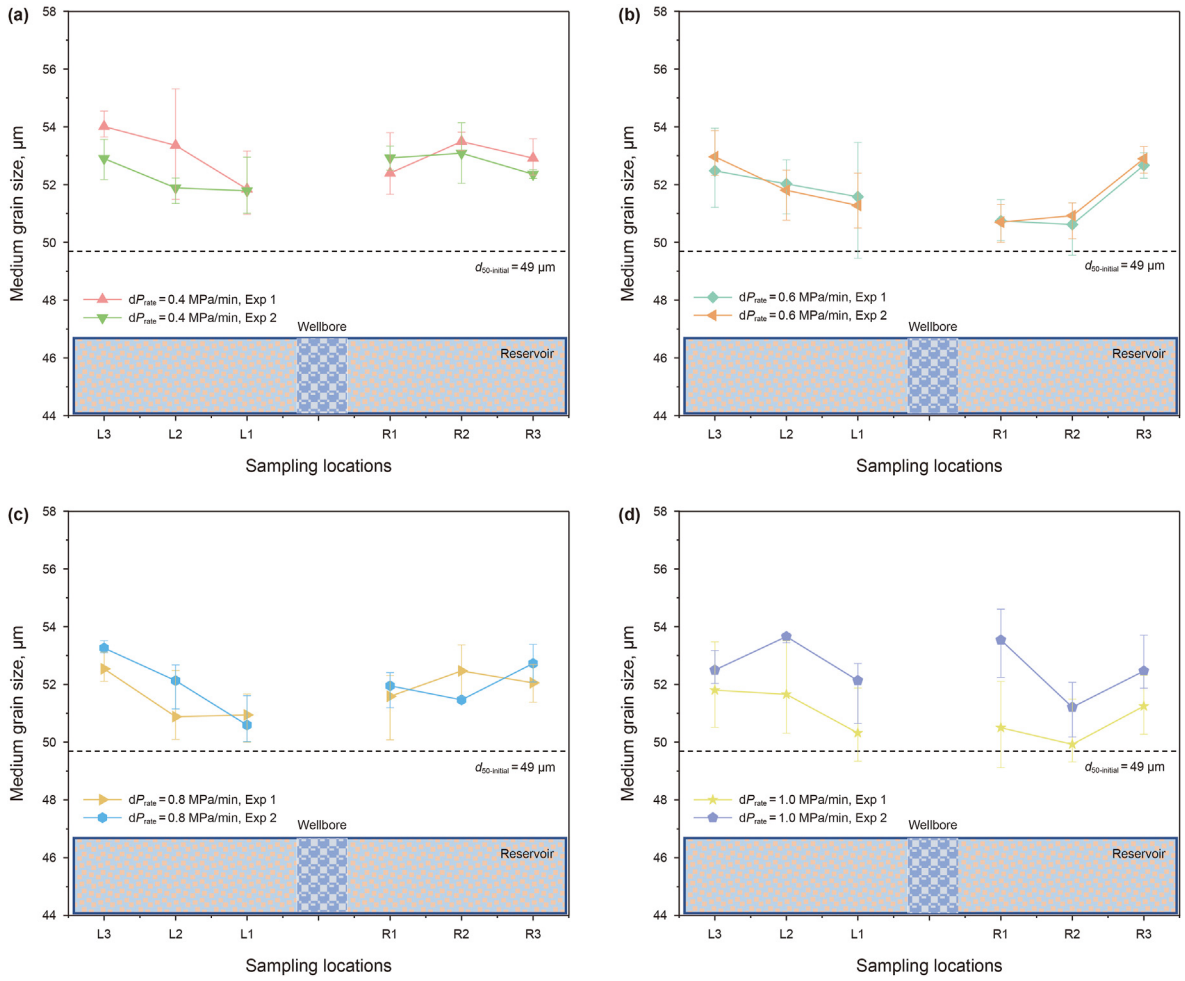

Fig. 19. Particle size distributions of the remnant sediment around the wellbore when initial MH saturation is 30%.

4. Implications on numerical modelling and field operation

4.1. How to bridge numerical simulation

Currently, most numerical simulation approaches attempt to predict sand production rate and cumulative sand, without considering the influence of particle migration regimes within the reservoir. Solid particles detached from the skeleton are usually supposed to flow within the porous media, and the structures of the skeleton are supposed to remain stable. However, the experimental results raise an interesting controversy: whether the solid particles migrate and flow out in a dispersed and isolated form in fluid or in the form of continuous flow. The current experiments revealed four optically visible sand failure regimes (i.e., local borehole failure, continuous collapse, wormhole expansion, extensive slow deformation) and one invisible sand migration regime (i.e., pore-wall fluidization) during MH dissociation by depressurization. The invisible pore-wall fluidization has been considered in the previous numerical models, whereas the constitutive models illustrating the visible particle migration regimes and their transmission modes remain to be developed. This might be the main inducement of discrepancies between the numerical results and field operational cases.

Another important phenomenon affecting solid migration and production behaviors during hydrate dissociation is the discontinuous and intermittent gas release from hydrate dissociation. The originally steady water flow could be heavily stirred by the gas bubble expansion and explosion, and thus the fluid flow regimes and directions change simultaneously. This phenomenon delays the solid particle outflow rate, and the delay-effect increases with the increase in initial MH hydrate. For this reason, an intermittent gas source term and a fluid-flow regime term shall be integrated into the sanding constitutive models. Some try to simulate sand production behaviors through experiments by taking tetrahydrofuran hydrate as a substitute. However, this is strongly not recommended based on our experiment, since the tetrahydrofuran hydrate dissociation does not include the intermittent gas source term.

4.2. Relationship between reservoir failure and sand production

We could conclude from the experiments that the sand failure area increases with the increase in initial MH saturation. However, both the cumulative mass and particle size of the produced sand decrease linearly with the increase in initial MH saturation. Besides, the depressurization rate is found to barely affect both solid migration regimes and produced sand, although the sand failure area could be enlarged by rapid depressurization. The experiments enlighten us that reservoir failure is a requirement for sand production, whereas reservoir failure is not equivalent to sand production. Mechanical constitutive models of the hydrate-bearing reservoirs cannot be used to describe sand production, even from a

qualitative perspective.

It was widely accepted that water flow dominates the sand production process during natural gas hydrate exploitation. As a result, some argue that the sand production rate and grain size of the produced sand increase with the increase in initial hydrate saturation. However, the current experiments yielded the opposite conclusions. The inconsistent results are proved to result from the intermittent gas bubble expansion and explosion, which interrupt the continuous water flow. From this view, the conclusion that water flow dominates the sand production process is an "imperfect" conclusion. Continuous water flow might be the main inducement of sand production, whereas discontinuous bubble release from hydrate dissociation delays sand production. The conclusion could also be validated by the comparative experiment stated in Section 3.2.2, from which depressurization was conducted in the sediment free of hydrate.

4.3. Implications on hydrate production strategies

The comparative experiments stated in Section 3.2.1 reveal that both the scale of the reservoir failure and the mass of the produced sand could be eased if no water drainage process is conducted after MH formation. This enlightens us that the sanding mechanisms of the water-saturated hydrate reservoir and gas-saturated hydrate reservoir are completely different. In a gas-saturated reservoir, the MH-dissociation released gas tends to be merged into the gas phase, forming a gas-dominant flow environment in the reservoir. Water shall be gasified in the gas-dominant environment and forms mist flow when gas flows into the wellbore. Forces applied by the pure gas and/or mist flow are much smaller than that applied by water, and thus, the sand production can be eliminated. However, a water-dominant environment shall be formed once the water drainage process is conducted. Bubble flow and/or slug flow shall be formed in such water-dominant environments. As a result, the sand production rate increases with the increase in water fraction in the flowing system.

The result enlightens us on mitigating sand production while extracting natural gas from marine hydrate reservoirs. On the one hand, the marine hydrate reservoir may be accompanied by an underlying gas layer (i.e., Class I hydrate reservoir). There is a transitional layer between the gas and the hydrate layers. Both the transitional layer and the underlying gas layer are gas-dominated. The gas-dominated intervals shall be perforated as a pay zone if the vertical well is deployed. In contrast, the horizontal section shall be laid in the gas-dominated layers if a horizontal well is deployed. Besides, it is possible to mitigate sand production by artificially changing the water-dominated environment into a gas-dominated one via special reservoir stimulation measurements, such as *in-situ* gas-water separation and gas injection.

5. Conclusions and suggestions

(1) Five particle migration regimes of local wellbore failure, continuous collapse, wormhole expansion, extensive slow deformation, and pore-wall fluidization, are proved to occur under different NGH saturation conditions during hydrate dissociation by depressurization. The types of particle migration regimes and their transmission modes are dominantly determined by initial hydrate saturation, whereas the depressurization mainly dominates the transmission rate of the particle migration regimes. In sediment with relatively high hydrate saturation, particles migrate in the form of local collapse, continuous collapse, extensive slow deformation, and relatively stable wormhole, successively. However, particle migration mode is proved to transfer from local collapse to wormhole expansion, extensive slow deformation, and secondary wormhole successively, when hydrate saturation is relatively low. The transmission rate would be accelerated obviously by increasing the depressurization rate.

(2) Both the cumulative mass and medium grain size of the produced sand decrease linearly with the increase in initial MH saturation, except that the cumulative mass and medium grain size of the produced sand from the experiments without MH are abnormally higher than those when the sediment contains MH in the initial state. The medium grain sizes of the produced sand are smaller than the original reservoir sediment by one order of magnitude. The depressurization is proved to have little influence on the produced sand's cumulative mass and medium grain size. Influencing mechanisms of the MH saturation on produced sand could be ascribed to discontinuous gas emission, expansion, and explosion during MH dissociation. In contrast, the influencing mechanisms of the depressurization rate on the produced sand are speculated to be related to the combination of intermittent gas release and hydrate reformation-induced blockage.

(3) Under the same depressurization rate, the medium grain size of the remnant sediment increases with the distance from the sampling locations to the simulated wellbore under relatively low initial MH saturation ($S_h = 0\%$, 7.5%, and 15%) conditions. However, the grain size of the remnant sediment decreases with the distance from the sampling locations to the simulated wellbore under relatively high initial MH saturation ($S_h = 30\%$, 45%, 60%, respectively) conditions. This implies that the sand failure area expands with the increase in MH saturation, although the cumulative produced sand decreases.

(4) Laboratory experiments provide insightful evidence to verify the numerical models and bridge the results with field operation. However, constitutive models illustrating the visible particle migration regimes and their transmission modes remain to be developed in the current state. The reservoir failure is a requirement for sand production, whereas reservoir failure is not equivalent to sand production. Continuous water flow is the primary cause of sand production, whereas discontinuous bubble release from hydrate dissociation delays sand production. It is possible to mitigate sand production tendency by optimizing wellbore layout positions or treating the reservoir to change the water-dominated environment into a gas-dominated one.

Conflict of interest

The authors declare that they have no known competing financial interests or personal relationships that could have appeared to influence the work reported in this paper.

Acknowledgement

This research was financially supported by the Laoshan Laboratory (No. LSKJ LSKJ202203506), the Taishan Scholars Program, and the National Natural Science Foundation of China (Grant No. 41976074).

References

Akaki, T., Kimoto, S., 2019. Numerical modelling of internal erosion during hydrate dissociation based on multiphase mixture theory. Int. J. Numer. Anal. Methods GeoMech. 44 (2), 327–350. https://doi.org/10.1002/nag.3023.

Bedrikovetsky, P., Zeinijahromi, A., Siqueira, F., et al., 2012. Particle detachment

under velocity alternation during suspension transport in porous media. Transport Porous Media 91, 173–197. https://doi.org/10.1007/s11242-011-9839-1.
Boswell, R., Collett, T.S., 2011. Current perspectives on gas hydrate resources. Energy Environ. Sci. 4, 1206–1215. https://doi.org/10.1039/C0EE00203H.
Chen, M., Li, Y., Merey, Ş., et al., 2022. Review on the test methods and devices for mechanical properties of hydrate-bearing sediments. Sustainability 14, 6239. https://doi.org/10.3390/su14106239.
Cui, Y., Lu, C., Wu, M., et al., 2018. Review of exploration and production technology of natural gas hydrate. Adv. Geo-Energy Res. 2, 53–62. https://doi.org/10.26804/ager.2018.01.05.
Ding, J., Cheng, Y., Yan, C., et al., 2019. Experimental study of sand control in a natural gas hydrate reservoir in the South China sea. Int. J. Hydrogen Energy 44, 23639–23648. https://doi.org/10.1016/j.ijhydene.2019.07.090.
Dong, C., Wang, L., Zhou, Y., et al., 2020. Microcosmic retaining mechanism and behavior of screen media with highly argillaceous fine sand from natural gas hydrate reservoir. J. Nat. Gas Sci. Eng. 83, 103618. https://doi.org/10.1016/j.jngse.2020.103618.
Dong, C., Zhou, Y., Chen, Q., et al., 2019. Effects of fluid flow rate and viscosity on gravel-pack plugging and the optimization of sand-control wells production. Petrol. Explor. Dev. 46, 1251–1259. https://doi.org/10.1016/S1876-3804(19)60278-8.
Dou, X., Ning, F., Li, Y., et al., 2020. Continuum-discrete coupling method for numerical simulation of sand production from hydrate reservoirs: a lab-scale study. Acta Pet. Sin. 41, 629–642. https://doi.org/10.7623/syxb202005011.
Fang, X., Ning, F., Wang, L., et al., 2021a. Dynamic coupling responses and sand production behavior of gas hydrate-bearing sediments during depressurization: an experimental study. J. Petrol. Sci. Eng. 201, 108506. https://doi.org/10.1016/j.petrol.2021.108506.
Fang, X., Yang, D., Ning, F., et al., 2021b. Experimental study on sand production and coupling response of silty hydrate reservoir with different contents of fine clay during depressurization. Petroleum 9 (1), 72–82. https://doi.org/10.1016/j.petlm.2021.11.008.
Han, G., Kwon, T., Lee, J., et al., 2018. Depressurization-induced fines migration in sediments containing methane hydrate: X-ray computed tomography imaging experiments. J. Geophys. Res. Solid Earth 123, 253–2558. https://doi.org/10.1002/2017JB014988.
Hancock, S., Boswell, R., Collett, T., 2019. Development of Deepwater Natural Gas Hydrates. 2019 Offshore Technology Conference. OTC program committee, Houston, Texas, USA, pp. 1–12. https://doi.org/10.4043/29374-MS.
Hu, Q., Li, Y., Sun, X., et al., 2023. Integrating test device and method for creep failure and ultrasonic response of methane hydrate-bearing sediments. Rev. Sci. Instrum. 94, 025105. https://doi.org/10.1063/5.0133198.
Jin, Y., Li, Y., Wu, N., et al., 2021. Characterization of sand production for clayey-silt sediments conditioned to openhole gravel-packing: experimental observations. SPE J. 26, 3591–3608. https://doi.org/10.2118/206708-PA.
Jin, Y., Wu, N., Li, Y., et al., 2022. Characterization of sand production for clayey-silt sediments conditioned to hydraulic slotting and gravel packing: experimental observations, theoretical formulations, and modeling. SPE J. 27, 3704–3723. https://doi.org/10.2118/209826-PA.
Li, J., Ye, J., Qin, X., et al., 2018a. The first offshore natural gas hydrate production test in South China Sea. China Geol. 1, 5–16. https://doi.org/10.31035/cg2018003.
Li, Y., Chen, M., Guang, S., et al., 2022a. "Ladetes"—a novel device to test deformation behaviors of hydrate-bearing sediments. Rev. Sci. Instrum. 93, 125004. https://doi.org/10.1063/5.0120205.
Li, Y., Cheng, Y.F., Yan, C.L., et al., 2022b. Effects of creep characteristics of natural gas hydrate-bearing sediments on wellbore stability. Petrol. Sci. 19 (1), 220–233. https://doi.org/10.1016/j.petsci.2021.10.026.
Li, Y., He, C., Wu, N., et al., 2021a. Laboratory study on hydrate production using a slow, multistage depressurization strategy. Geofluids 2021, 4352910. https://doi.org/10.1155/2021/4352910.
Li, Y., Hu, G., Liu, C., et al., 2017. Gravel sizing method for sand control packing in hydrate production test wells. Petrol. Explor. Dev. 44, 1016–1021. https://doi.org/10.1016/S1876-3804(17)30114-3.
Li, Y., Liu, C., Liu, L., et al., 2018b. Experimental study on evolution behaviors of triaxial-shearing parameters for hydrate-bearing intermediate fine sediment. Adv. Geo-Energy Res. 2 (1), 43–52. https://doi.org/10.26804/ager.2018.01.04.
Li, Y., Liu, L., Liu, C., et al., 2016. Sanding prediction and sand-control technology in hydrate exploitation: a review and discussion. Marine Geol. Front. 32 (7), 36–43. https://doi.org/10.16028/j.1009-2722.2016.07005 (in Chinese).
Li, Y., Ning, F., Wu, N., et al., 2020. Protocol for sand control screen design of production wells for clayey silt hydrate reservoirs: a case study. Energy Sci. Eng. 8, 1438–1449. https://doi.org/10.1002/ese3.602.
Li, Y., Wu, N., Gao, D., et al., 2021b. Optimization and Analysis of Gravel Packing Parameters in Horizontal Wells for Natural Gas Hydrate Production. Energy, 119585. https://doi.org/10.1016/j.energy.2020.119585.
Li, Y., Wu, N., Ning, F., et al., 2019. A sand-production control system for gas production from clayey silt hydrate reservoirs. China Geology 2, 1–13. https://doi.org/10.31035/cg2018081.
Liu, X.H., Hu, T., Pang, X.Q., et al., 2022. Evaluation of natural gas hydrate resources in the South China Sea using a new genetic analogy method. Petrol. Sci. 19 (1), 48–57. https://doi.org/10.1016/j.petsci.2021.12.004.
Liu, Y., Hou, J., Zhao, H., et al., 2018. A method to recover natural gas hydrates with geothermal energy conveyed by CO_2. Energy 144, 265–278. https://doi.org/10.1016/j.energy.2017.12.030.
Lu, J., Xiong, Y., Li, D., et al., 2019a. Experimental study on sand production and seabottom subsidence of non-diagenetic hydrate reservoirs in depressurization production. Mar. Geol. Quat. Geol. 39 (4), 183–195. https://doi.org/10.16562/j.cnki.0256-1492.2019012301 (in Chinese).
Lu, R., Stern, L.A., Du Frane, W.L., et al., 2019b. The effect of brine on the electrical properties of methane hydrate. JGR Solid Earth 124, 10877–10892. https://doi.org/10.1029/2019JB018364.
Makogon, Y.F., 2010. Natural gas hydrates—A promising source of energy. J. Nat. Gas Sci. Eng. 2 (1), 49–59. https://doi.org/10.1016/j.jngse.2009.12.004.
Merey, Ş., 2019. Evaluation of drilling parameters in gas hydrate exploration wells. J. Petrol. Sci. Eng. 172, 855–877. https://doi.org/10.1016/j.petrol.2018.08.079.
Murphy, A., Soga, K., Yamamoto, K., 2020. Experimental investigation into sand production from turbidite strata. J. Petrol. Sci. Eng. 190, 107056. https://doi.org/10.1016/j.petrol.2020.107056.
Ning, F., Dou, X., Sun, J., et al., 2020. Progress in numerical simulation of sand production from hydrate reservoirs. Petroleum Science Bulletin 5, 182203. https://doi.org/10.3969/j.issn.2096-1693.2020.02.018 (in Chinese).
Oyama, H., Nagao, J., Suzuki, K., et al., 2010. Experimental analysis of sand production from methane hydrate bearing sediments applying depressurization method. Journal of MMIJ 126, 497–502. https://doi.org/10.2473/journalofmmij.126.497.
Qi, M., Li, M., Moghanloo, G.R., et al., 2021. A novel simulation approach for particulate flows during filtration. AIChE J. 67, e17136. https://doi.org/10.1002/aic.17136.
Qi, M., Li, Y., Moghanloo, R.G., et al., 2022. A novel approach to predict sand production rate through gravel packs in unconsolidated sediment applying the theory of free fall arch. SPE J. 28, 415–428. https://doi.org/10.2118/210602-PA.
Riley, D., Marin-Moreno, H., Minshull, T.A., 2019. The effect of heterogeneities in hydrate saturation on gas production from natural systems. J. Petrol. Sci. Eng. 183, 106452. https://doi.org/10.1016/j.petrol.2019.106452.
Shen, S., Li, Y., Sun, X., et al., 2021. Analysis of the mechanical properties of methane hydrate-bearing sands with various pore pressures and confining pressures. J. Nat. Gas Sci. Eng. 87, 103786. https://doi.org/10.1016/j.jngse.2020.103786.
Uchida, S., Klar, A., Yamamoto, K., 2016. Sand production model in gas hydrate-bearing sediments. Int. J. Rock Mech. Min. Sci. 86, 303–316. https://doi.org/10.1016/j.ijrmms.2016.04.009.
Uchida, S., Lin, J.S., Myshakin, E.M., et al., 2019. Numerical simulations of sand migration during gas production in hydrate-bearing sands interbedded with thin mud layers at site NGHP-02-16. Mar. Petrol. Geol. 108, 639–647. https://doi.org/10.1016/j.marpetgeo.2018.10.046.
Wang, D., Liu, Z., Ning, F., et al., 2020. Dynamic responses of THF hydrate-bearing sediments under small strain: resonance column test. J. Nat. Gas Sci. Eng. 81, 103399. https://doi.org/10.1016/j.jngse.2020.103399.
Wang, H., Wu, P., Li, Y., et al., 2023. Gas permeability variation during methane hydrate dissociation by depressurization in marine sediments. Energy 263 (Part B), 125749. https://doi.org/10.1016/j.energy.2022.125749.
Wu, N., Li, Y., Chen, Q., et al., 2021a. Sand production management during marine natural gas hydrate exploitation: review and an innovative solution. Energy Fuel. 35, 4617–4632. https://doi.org/10.1021/acs.energyfuels.0c03822.
Wu, N., Li, Y., Wan, Y., et al., 2021b. Prospect of marine natural gas hydrate stimulation theory and technology system. Nat. Gas. Ind. B 8, 173–187. https://doi.org/10.1016/j.ngib.2020.08.003.
Wu, P., Li, Y., Wang, L., et al., 2022. Hydrate-bearing sediment of the South China sea: microstructure and mechanical characteristics. Eng. Geol. 307, 106782. https://doi.org/10.1016/j.enggeo.2022.106782.
Yamamoto, K., Terao, Y., Fujii, T., 2014. Operational Overview of the First Offshore Production Test of Methane Hydrates in the Eastern Nankai Trough. Offshore Technology Conference, Houston, Texas, USA. https://doi.org/10.4043/25243-MS, 2014.
Yamamoto, K., Wang, X., Tamaki, M., et al., 2019. The second offshore production of methane hydrate in the Nankai Trough and gas production behavior from a heterogeneous methane hydrate reservoir. RSC Adv. 9, 25987–26013. https://doi.org/10.1039/C9RA00755E.
Yang, Y., He, Y., Zheng, Q., 2017. An analysis of the key safety technologies for natural gas hydrate exploitation. Adv. Geo-Energy Res. 1, 100–104. https://doi.org/10.26804/ager.2017.02.05.
Ye, J., Qin, X., Xie, W., et al., 2020. The second offshore natural gas hydrate production test in South China Sea. China Geology 3, 197–209. https://doi.org/10.31035/cg2018003.
Yoshihiro, T., Mike, D., Bill, H., et al., 2014. Deepwater Methane Hydrate Gravel Packing Completion Results and Challenges. Offshore Technology Conference, Houston, Texas, USA. https://doi.org/10.4043/25330-MS.
Yu, T., Liu, Y., Song, Y., 2020. Experimental study on sand production characteristics in natural gas hydrate deposits. IOP Conf. Ser. Earth Environ. Sci. 446, 052056. https://doi.org/10.1088/1755-1315/446/5/052056.
Zhang, Z., Li, C., Ning, F., et al., 2020. Pore practal characteristics of hydrate-bearing sands and implications to the saturated water permeability. JGR Solid Earth 125, e2019JB018721. https://doi.org/10.1029/2019JB018721.
Zhu, H., Xu, T., Yuan, Y., et al., 2020. Numerical investigation of the natural gas hydrate production tests in the Nankai Trough by incorporating sand migration. Appl. Energy 275, 115384. https://doi.org/10.1016/j.apenergy.2020.115384.